Chemical Engineering Journal 319 (2017) 229–239

Contents lists available at ScienceDirect

Chemical Engineering Journal

journal homepage: www.elsevier.com/locate/cej

Different approaches for preparing a novel thiol-functionalized graphene oxide/Fe-Mn and its application for aqueous methylmercury removal

Yao Huang [a], Jingchun Tang [a,*], Longshuang Gai [a], Yanyan Gong [b,*], Hongwei Guan [c], Ruozhu He [a], Honghong Lyu [a]

[a] College of Environmental Science and Engineering, Key Laboratory of Pollution Processes and Environmental Criteria (Ministry of Education), Tianjin Engineering Center of Environmental Diagnosis and Contamination Remediation, Nankai University, Tianjin 300350, China
[b] School of Environment, Guangzhou Key Laboratory of Environmental Exposure and Health, and Guangdong Key Laboratory of Environmental Pollution and Health, Jinan University, Guangzhou 510632, China
[c] Water Environmental Restoration Research Center, College of Architecture and Civil Engineering, Beijing University of Technology, Beijing 100124, China

HIGHLIGHTS

- Thiol-functionalized graphene oxide/Fe-Mn composite synthesized via three methods.
- Composite formed via interaction between 3-MPTS and GO/Fe-Mn and self-polymerization.
- Ammonium hydroxide method obtains the composite with highest sorption capacity.
- CH_3Hg^+ removed by electrostatic attraction, ligand exchange and surface complexation.

GRAPHICAL ABSTRACT

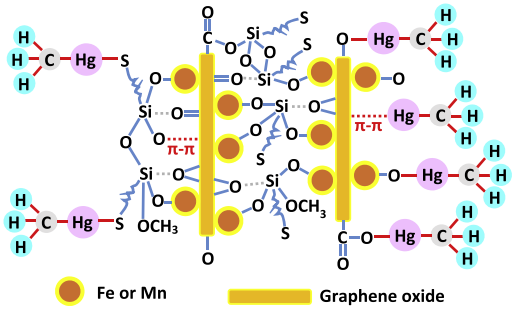

SGO/Fe-Mn formation mechanism:
O=C-O, C-O-C, C=O, C-O, π-π interactions, and 3-MPTS self-polymerization

Methylmercury removal mechanism:
Electrostatic attraction, ligand exchange, and surface complexation

ARTICLE INFO

Article history:
Received 5 January 2017
Received in revised form 4 March 2017
Accepted 6 March 2017
Available online 8 March 2017

Keywords:
Methylmercury sorption
Thiol-functionalized graphene oxide/Fe-Mn
3-Mercaptopropyltrimethoxysilane (3-MPTS)

ABSTRACT

A novel thiol-functionalized graphene oxide/Fe-Mn composite (SGO/Fe-Mn) was synthesized via three different methods, i.e., acetic acid method (SGO/Fe-Mn-ac), neutral method (SGO/Fe-Mn-ne), and ammonium hydroxide method (SGO/Fe-Mn-am). The composites were characterized and tested for aqueous methylmercury removal. SGO/Fe-Mn was prepared using 3-mercaptopropyltrimethoxysilane (3-MPTS) as a silanizing reagent, and hydrolyzed 3-MPTS mainly interacted with GO/Fe-Mn through surface oxygen-containing groups (i.e., —OH, C=O, epoxy C—O—C, carboxyl O=C—O, and C—O) and π-π interactions, partially through self-polymerization. SGO/Fe-Mn-am showed the largest hydrodynamic diameter, strongest π-π bond, fewest S oxidation products, most thiol groups, negative charge, sp^3 defects, and FeOOH. Pseudo-second-order kinetic model and Langmuir and Freundlich isotherm models fitted well with methylmercury sorption kinetic and isotherm data, respectively, resulting in a CH_3Hg^+ maximum sorption capacity of 43.88 mg/g for SGO/Fe-Mn-am, 36.33 mg/g for SGO/Fe-Mn-ac, and 28.00 mg/g for SGO/Fe-Mn-ne. The removal mechanism was described by electrostatic attraction, ligand exchange, and surface complexation. This study demonstrates potential and viability of SGO/Fe-Mn for enhanced immobilization of CH_3Hg^+ in surface water, groundwater, and soil/sediments.

1. Introduction

Industrial activities, such as paints, pulp, oil refining, rubber processing, fertilizer, batteries, thermometers, fluorescent light

* Corresponding authors.
E-mail addresses: tangjch@nankai.edu.cn (J. Tang), yanyangong@jnu.edu.cn (Y. Gong).

http://dx.doi.org/10.1016/j.cej.2017.03.015
1385-8947/

tubes, high intensity street lamps, pesticides, cosmetics, and pharmaceuticals are primary anthropogenic sources of mercury emissions [1,2]. Methylmercury (CH_3Hg^+) is the most toxic form of mercury. It is primarily formed by anaerobic sulfate- and iron-reducing bacteria and methanogenic archaea in anoxic sediments and wetland soils [3,4]. CH_3Hg^+ is a known potent neurotoxin and it tends to bioaccumulate and biomagnify over the food chain, where concentrations can reach one million times greater than in aquatic environment [5]. For human beings, CH_3Hg^+ exposure occurs predominantly through the consumption of aquatic products (e.g., freshwater and marine varieties, shellfish, and marine mammals), and prolonged exposure can cause deleterious effects, such as renal disorders and acute myocardial infarction [6,7]. CH_3Hg^+ is particularly harmful to brain (e.g. deficits in fine motor skills, language, and memory) and can cause irreversible damage to the central nervous system [7]. World Health Organization (WHO) and United States Environmental Protection Agency (USEPA) recommends a maximum CH_3Hg^+ intake of 1.6 μg/kg body weight per week and 0.1 μg/kg per day, respectively [8,9].

Several techniques have been applied for CH_3Hg^+ removal from water, including photodegradation [6], biodegradation [10], coagulation [11], and adsorption [2,12–17]. Adsorption is recognized as one of the most promising approaches in terms of its low cost, ease of operation, and simplicity of design [18]. However, up to now, the reported sorbents for CH_3Hg^+ removal are few, mainly including chitosan and its derivatives (e.g., barbital immobilized/cross-linked with chitosan) [2,12], biosorbents (e.g., *Lemna minor* powder, *Coriandrum sativum*, and rasped pith *sago* residue) [13–15], and metal oxide composites (e.g., FeOOH and divinylbenzene polymer/Fe_3O_4) [16,17]. However, most of the adsorbents bear with several disadvantages, such as low adsorption capacity and weak binding affinity for CH_3Hg^+. To overcome these disadvantages, it is necessary to explore adsorbent materials with good removal performance and selectivity for CH_3Hg^+.

Thiol-functionalized adsorbents have drawn a lot of attention recently since they exhibit a high adsorption capacity and a strong binding affinity for Hg^{2+} and CH_3Hg^+, as a consequence of a soft Lewis acid-base interaction [19]. Kazemi et al. [20] developed a thiol-incorporated activated carbon (produced from fir wood sawdust). The resultant material possessed a higher Hg^{2+} maximum monolayer adsorption capacity (129 mg/g) than raw activated carbon (107 mg/g) with initial Hg^{2+} concentrations of 10–110 mg/L, pH of 6, a dosage of 0.5 g/L, and equilibrium time of 120 min. Kumar et al. [21] reported that thiol-functionalized graphene oxide was an effective adsorbent for CH_3Hg^+ with a maximum Langmuir sorption capacity of 48.07 mg/g, and 5 g/L adsorbent removed 98.50% of 30 mg/L CH_3Hg^+ at pH 5.4–6.9 within 30 min.

3-Mercaptopropyltrimethoxysilane (3-MPTS) is a widely used thiol-modification chemical [18,22–25]. 3-MPTS can hydrolyze at certain conditions, the hydrolyzable methoxy group is desorbed as methanol, and the remaining part of 3-MPTS can dehydrate/ligand exchange with hydroxyl groups on the surface of raw materials (e.g., metal oxides, smectite, and SiO_2) [22–24], or forming a strong interfacial adhesion with surface oxygen containing groups (e.g., C—O, carboxyl O═C—O) [13,25]. Our previous work [26] demonstrated that graphene oxide/Fe-Mn (GO/Fe-Mn) possessed several advantages over graphene oxide (GO), namely, (1) more abundant functional groups (e.g., hydroxyl) on the surface, providing more active sites for surface thiol-modification; (2) easier separation from aqueous solution; and (3) better biocompatibility. Preliminary experiments showed that 50 mg/L GO/Fe-Mn only removed 17.10% of 50 μg/L methylmercury from aqueous solution at pH of 7 within 3 days. In this study, 3-MPTS, a common silanizing reagent, was chosen to modify GO/Fe-Mn to obtain thiol-functionalized GO/Fe-Mn (SGO/Fe-Mn) for the first time for aqueous methylmercury removal. Preliminary tests showed that SGO/Fe-Mn can be completely separated from aqueous solution within 30 min by gravity, while it took 7 h for complete separation of thiol-functionalized graphene oxide (SGO), i.e., the introduction of Fe-Mn particles led to a better separation performance. The specific objectives were to: (1) synthesize a novel SGO/Fe-Mn via three prevalent methods, i.e., acetic acid method, neutral method, and ammonium hydroxide method; (2) compare the physicochemical properties of three SGO/Fe-Mn and elucidate the formation mechanisms; and (3) examine their removal effectiveness for aqueous CH_3Hg^+ and explore the possible removal mechanism.

2. Materials and methods

2.1. Chemicals

All chemicals used in this study were of analytical grade or better. Methylmercury chloride (CH_3HgCl) (97%) was provided by Dr. Ehrenstorfer GmbH (Augsburg, Germany). 3-MPTS (97%) and ethanol (HPLC grade) were purchased from J&K Scientific (Beijing, China). Graphene oxide (GO) (98%) was obtained from Tianjin Ailian Electronic Technology (Tianjin, China). Sulfate heptahydrate ($FeSO_4{\cdot}7H_2O$) (analytical grade), potassium permanganate ($KMnO_4$) (analytical grade), potassium hydroxide (KOH) (guaranteed grade), potassium borohydride (KBH_4) (guaranteed grade), acetic acid (CH_3COOH) (analytical grade), ammonium hydroxide solution (NH_4OH) (25% NH_3 in H_2O) (analytical grade), nitric acid (HNO_3) (guaranteed grade), and sodium hydroxide (NaOH) (analytical grade) were procured from Tianjin Chemical Reagent Technology (Tianjin, China). A stock solution of 1000 mg Hg/L CH_3HgCl solution was prepared using HPLC grade methanol (J&K Scientific, Beijing, China), and working solutions were diluted appropriately with ultrapure water.

2.2. Preparation of GO/Fe-Mn

GO/Fe-Mn composite was prepared following our previous method [26]. Briefly, GO suspensions (2 g/L), solutions of $KMnO_4$ (9.58×10^{-4} M) and $FeSO_4$ (2.87×10^{-3} M) were prepared with N_2-purged ultrapure water. Then, 6 mL $FeSO_4$ and 18 mL GO solutions were added to 270 mL ultrapure water under vigorous magnetic stirring. Subsequently, 6 mL $KMnO_4$ solution were introduced into the mixed solution dropwise and pH of the suspension was adjusted to 7.5 with HNO_3 (1 M and 0.1 M) and NaOH (1 M and 0.1 M). The mixture was continuously stirred for another 1 h and aged at 25 ± 2 °C for 12 h to allow the full growth of the particles. After freeze-drying under vacuum at −60 °C (FD5-3 freeze-dryer, SIM, California, USA) for 48 h, GO/Fe-Mn powder was obtained.

2.3. Preparation of SGO/Fe-Mn

SGO/Fe-Mn were prepared via three revised approaches, namely, acetic acid method [18], neutral method [27], and ammonium hydroxide method [22] (Fig. 1). Briefly, 150 mg of GO/Fe-Mn powder was washed with ethanol for three times, dispersed in 20 ml of toluene by immersing the flask in an ultrasonic bath (270 W) for 1 h, and stirred for another 1 h. The particles were then washed with ethanol (150 mL), and diluted to 300 mL with 2% 3-MPTS in 95% ethanol under anaerobic conditions. For acetic acid method, pH of the mixture was adjusted to 4.5 via the addition of 16 mmol/L acetic acid (CH_3COOH), followed by mixing and heating at 60 °C for 3 h. For neutral method, the mixture with a measured pH value of 7.0 was stirred and heated at 60 °C for 3 h. For ammonium hydroxide method, after 6 h, pH was adjusted to 9.5 by NH_4OH and the mixture continuously reacted for an additional 24 h. Subsequently, for all the three approaches, the particles were

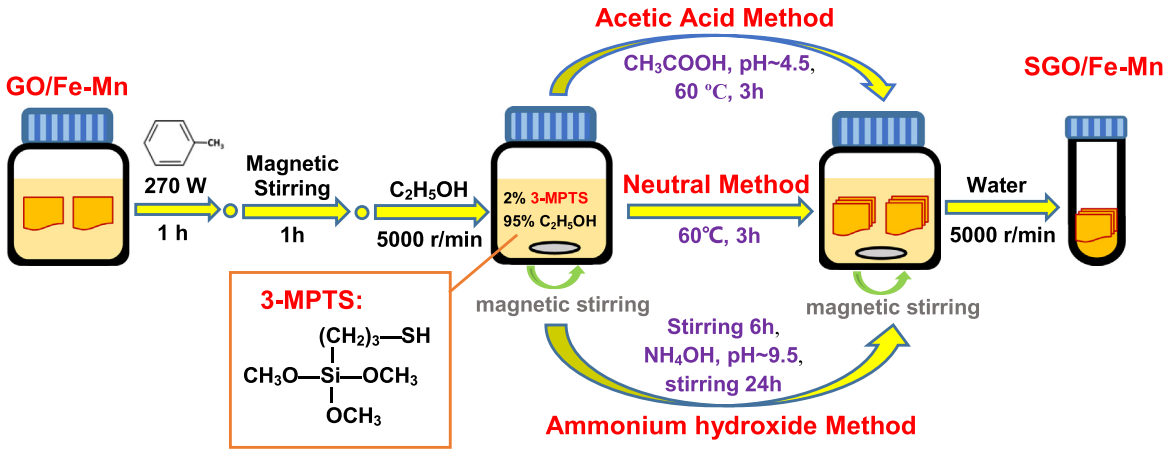

Fig. 1. Preparation of SGO/Fe-Mn via three methods.

separated by centrifugation and washed with 300 mL deionized water. After freeze-drying under vacuum at −60 °C for 48 h, SGO/Fe-Mn were obtained. The three resultant materials were named as SGO/Fe-Mn-ac (acid method), SGO/Fe-Mn-ne (neutral method), and SGO/Fe-Mn-am (ammonium hydroxide method), respectively.

2.4. Characterization

Hydrodynamic diameter and zeta potential (ζ) of SGO/Fe-Mn were determined by dynamic light scattering (DLS) tests using a Malvern Zeta sizer Nano ZEN3690 Instrument (Malvern Instruments, Worcestershire, UK). Suspensions (100 mg/L) of GO/Fe-Mn and SGO/Fe-Mn were prepared by ultrasonic dispersion for 40 min (500 W) using a KQ-500B ultrasonic cleaner (Kunshanshumei, Jiangsu, China). Fourier transform infrared (FTIR) analysis was conducted by a FTS-6000 spectrometer (Bio-rad, California, USA) to explore interactions between 3-MPTS and GO/Fe-Mn, and the resolution is 4 cm^{-1}. Samples were mixed with KBr (spectroscopy grade) powders and pressed into tablets for characterization. Transmission electron microscopy (TEM) measurements were performed with a Tecnai G2 F20 microscope (FEI, Hillsboro, USA). Samples were dispersed in ethanol with ultra-sonication for 30 min, placed on a formvar-carbon coated copper grid, and allowed for full drying. The residual particles attached to the grid were applied for TEM analysis. Raman spectra were carried out on a Renishaw inVia Raman microscope system (Renishaw, Gloucestershire, UK) using a 514.5 nm argon ion laser, and the resolution is 1 cm^{-1}. Surface elemental compositions were analyzed by X-ray photoelectron spectroscopy (XPS) using a PHI-5000 Versaprobe II spectrometer (ULVAC-PHI, Chigasaki, Japan) with a Kα-Al radiation ($h\nu$ = 1486.6 eV). Energy step size was 0.05 eV for each element scan and 1.0 eV for a wide scan, and pass energy was 20.0 eV and 100.0 eV, respectively. XPS spectra were analyzed using CasaXPS software (version 2.3.18) [28] with Gaussian (Y%)-Lorentzian (X%) profiles defined in CasaXPS as GL (X) [29]. Line shapes of GL (30) were used for individual components (i.e., C1s, O1s, Fe2p, Mn2p, S2p and Si2p). Surface areas were determined by the Brunauer-Emmett-Tuller (BET) N_2 adsorption method (ASAP2460, Micromeritics, Atlanta, USA).

2.5. CH_3Hg^+ sorption tests

CH_3Hg^+ sorption kinetic and isotherm tests by GO/Fe-Mn and three types of SGO/Fe-Mn were assessed in sealed 30 mL PTFE vials. The experimental conditions were: $NaNO_3$ = 0.01 M, pH = 7.0 ± 0.2, and adsorbent dosage = 50 mg/L. It should be noted that 0.01 M $NaNO_3$ was added to keep a constant ionic strength [18,26,30]. The reaction was initiated by adding a certain volume of CH_3Hg^+ solution in the SGO/Fe-Mn suspensions. The vials were then sealed and agitated on an end-over-end rotator at 40 rpm at room temperature (25 ± 2 °C). After the reaction, samples were centrifuged at 5000 rpm for 10 min, and the supernatant was analyzed for aqueous methylmercury.

For sorption kinetic experiments, the initial concentration of CH_3Hg^+ was 50 μg Hg/L, and CH_3Hg^+ removal was followed for 72 h by measuring aqueous CH_3Hg^+ remaining. For sorption isotherm tests, the initial CH_3Hg^+ concentration varied from 50 to 950 μg Hg/L, and the vials were equilibrated for 72 h. Control tests in the absence of adsorbents showed that loss of CH_3Hg^+ during the experiments was <4% for all cases. All experiments were performed in duplicate.

2.6. Analytical methods

pH value was measured using a PB-10 pH meter (Sartorius, Gottingen, Germany). CH_3Hg^+ concentration was determined using an AFS-830 atomic fluorescence spectrometer (Titan Instruments, Beijing, China) following the Environmental Protection Standards of People's Republic of China (HJ694-2014). The detection limit was 0.04 μg Hg/L.

3. Results and discussion

3.1. Characterization of SGO/Fe-Mn composites and synthesis mechanisms

Fig. 2 compares TEM images of GO/Fe-Mn and SGO/Fe-Mn-am. As discussed in our previous research [26], for GO/Fe-Mn, Fe-Mn particles were distributed on the surface of GO. GO/Fe-Mn showed a sheet structure while SGO/Fe-Mn particles significantly aggregated together due to the bridging by 3-MPTS. BET measurement further confirmed the bridging, SGO/Fe-Mn had a smaller BET surface area than GO/Fe-Mn (Table S1). For instance, the BET surface area of SGO/Fe-Mn-am was 2.79 m^2/g, which was smaller than 1.53 × 10^2 m^2/g for GO/Fe-Mn [26]. DLS measurements conducted at pH 7 showed an increase in the hydrodynamic diameters of three SGO/-Fe-Mn (816 ± 12 nm for SGO/Fe-Mn-ac, 781 ± 15 nm for SGO/Fe-Mn-ne, and 855 ± 20 nm for SGO/Fe-Mn-am), compared to GO/Fe-Mn (350 ± 20 nm) [26].

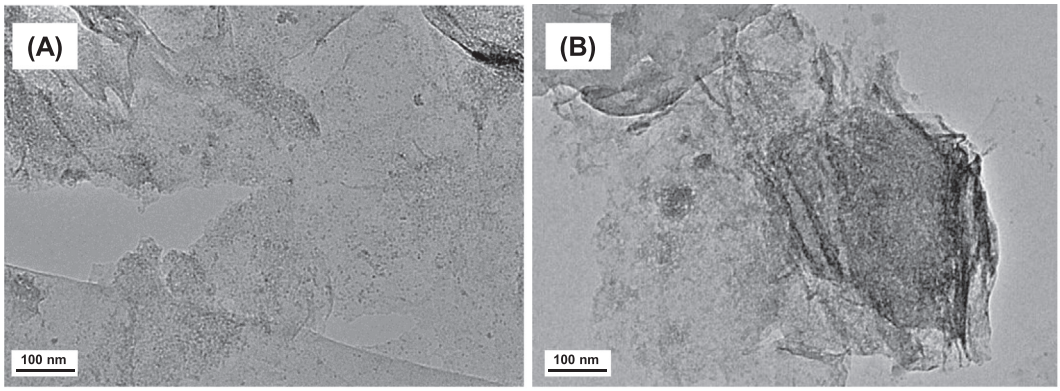

Fig. 2. TEM images of (A) GO/Fe-Mn [26] and (B) SGO/Fe-Mn-am.

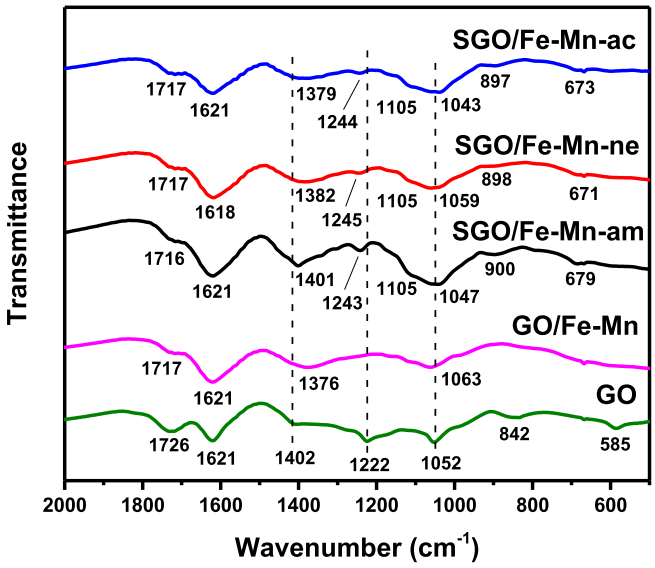

Fig. 3. FTIR spectra of GO, GO/Fe-Mn [26], and three SGO/Fe-Mn.

Figs. 3 and S1 compare the surface functional groups of GO, GO/Fe-Mn, and SGO/Fe-Mn. For GO, the peaks at 3400, 1726, 1402, 1222, 1052 and 1621 cm^{-1} are ascribed to the vibration of —OH, C═O, carboxyl O═C—O/tertiary C—OH, epoxy C—O—C, C—O groups, and C═C stretching vibration of sp^2 carbon skeletal network [31–33]. Compared with GO, the C═O and epoxy C—O—C intensity of GO/Fe-Mn diminished, C═C increased, the carboxyl O═C—O and C—O stretching band shifted [26]. For SGO/Fe-Mn-ac, SGO/Fe-Mn-ne, and SGO/Fe-Mn-am, C—S stretching vibration was observed at 673, 671, and 679 cm^{-1}, C—O/Si—O—M (M = Si, Fe, or Mn) at 1043, 1059, and 1047 cm^{-1}, and —CH_2 stretching vibration at 2924, 2920, and 2924 cm^{-1}, respectively [22]. Si—C stretching band was observed at 1105 cm^{-1} and S–H stretching vibration was weak and broadened at 2600–2550 cm^{-1} for all the three SGO/Fe-Mn [22,34]. The hydrolyzable methoxy group (—OCH_3) in 3-MPTS may be desorbed as methanol during the formation of SGO/Fe-Mn [23].

Compared with GO/Fe-Mn, all the functional groups (i.e., —OH, C═O, carboxyl O═C—O, epoxy C—O—C, C—O groups, and C═C) existed in SGO/Fe-Mn. Carboxyl O═C—O/tertiary C—OH band shifted from 1376 cm^{-1} for GO/Fe-Mn to 1382 cm^{-1} for SGO/Fe-Mn-ne and 1401 cm^{-1} for SGO/Fe-Mn-am, respectively. C—O stretching band shifted from 1063 cm^{-1} for GO/Fe-Mn [26] to 1043 and 1047 cm^{-1} for SGO/Fe-Mn-ac and SGO/Fe-Mn-am, respectively. The GO band at 1222 cm^{-1} (epoxy C—O—C) disappeared in GO/Fe-Mn while shifted to 1244, 1243, and 1245 cm^{-1} for SGO/Fe-Mn-ac, SGO/Fe-Mn-am, and SGO/Fe-Mn-ne, respectively. All these changes confirmed that 3-MPTS interacted with the GO/Fe-Mn surface forming a robust coating through oxygen-containing functional groups (i.e., hydroxyl, epoxy C—O—C, carboxyl O═C—O, and C—O). Among the three thiol-functionalized materials, SGO/Fe-Mn-am has the maximum peak intensities at 1621 cm^{-1} (C═C), 1401 cm^{-1} (carboxyl O═C—O/tertiary C—OH), 1243 cm^{-1} (epoxy C—O—C), and 1047 cm^{-1} (C—O), indicating more active sites.

Fig. 4 shows that GO/Fe-Mn and three SGO/Fe-Mn were negatively charged at pH range of 3–9, which was beneficial to CH_3Hg^+ removal by electrostatic attraction. SGO/Fe-Mn showed higher ζ potential than GO/Fe-Mn probably due to the occupation of negatively charged functional groups (e.g., —OH, carboxyl O═C—O and C—O) on the surface of GO/Fe-Mn by hydrolyzed 3-MPTS. Moreover, the hydrolyzed 3-MPTS can not only combine with the surface active sites, but also undergo self-polymerization to form a polymer [22,25]. For instance, at pH = 7, ζ potential was −37.73 ± 1.25 mV for GO/Fe-Mn [26], while less negatively charged for SGO/Fe-Mn, which followed the order of SGO/Fe-Mn-am (−33.93 ± 0.83 mV) < SGO/Fe-Mn-ac (−25.33 ± 0.65 mV) < SGO/Fe-Mn-ne (−22.93 ± 0.03 mV).

Raman spectra of GO, GO/Fe-Mn, and three SGO/Fe-Mn are shown in Fig. 5. Two characteristic peaks of GO at 1353 and

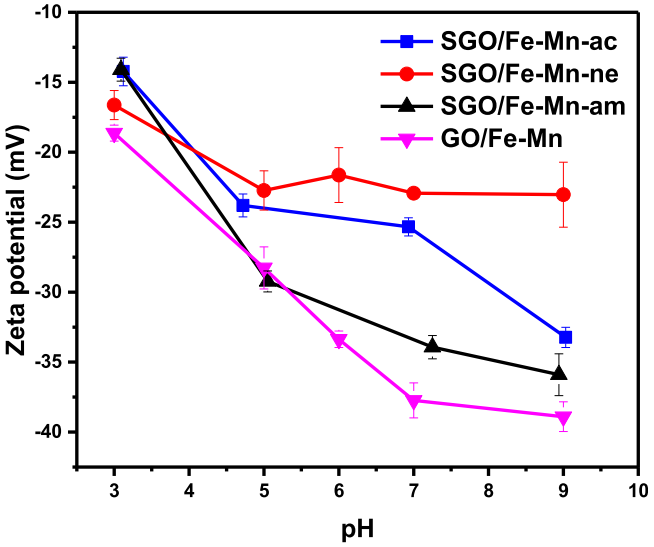

Fig. 4. Zeta potential of GO/Fe-Mn [26] and three SGO/Fe-Mn.

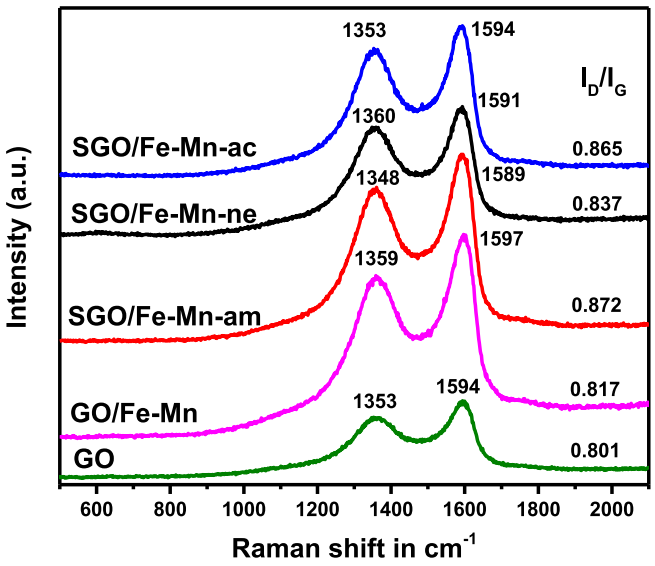

Fig. 5. Raman spectra of GO, GO/Fe-Mn [26] and three SGO/Fe-Mn.

1594 cm^{-1} were observed corresponding to the D-band (structural defects or partially disordered structures of sp^3 domains) and G-band (in-plane vibrational mode of sp^2 domains, which include sp^2 C=C stretch vibrations) [35]. D/G band was slightly shifted from 1359/1597 cm^{-1} for GO/Fe-Mn [26] to 1353/1594, 1360/1591, and 1348/1589 cm^{-1} for SGO/Fe-Mn-ac, SGO/Fe-Mn-ne, and SGO/Fe-Mn-am, respectively. The shift can be ascribed to the degree of electronegativity change or steric strain due to the 3-MPTS coating on the surface of SGO/Fe-Mn [36]. Furthermore, the intensity ratios of D and G band (I_D/I_G) of SGO/Fe-Mn samples were higher than GO/Fe-Mn and GO: SGO/Fe-Mn-am (0.872) > SGO/Fe-Mn-ac (0.865) > SGO/Fe-Mn-ne (0.837) > GO/Fe-Mn (0.817) [26] > GO (0.801), indicating that SGO/Fe-Mn (especially SGO/Fe-Mn-am) contained more defects and a significant increase in disordered carbon due to the surface functionalization [37]. FTIR results showed that, after thiol modification by 3-MPTS, more sp^3-type groups (e.g., C—C, C—S, and C—Si) were introduced onto the surface of SGO/Fe-Mn, and the peaks of original sp^2-type groups (e.g., C—O—C, C=O, and O=C–O) shifted, which correlated with the shifts of D band and the increase of I_D/I_G ratio in SGO/Fe-Mn [38,39]. In addition, the shifts of G band may be associated with π-π interactions during the thiol modification process [38].

Fig. S2 showed the XPS wide scan of GO/Fe-Mn and three SGO/Fe-Mn in which C1s, O1s, Fe2p, Mn2p, S2p and Si2p are clearly observed. Table 1 compares the atomic percentage of GO/Fe-Mn and the three SGO/Fe-Mn. SGO/Fe-Mn-am contained the highest thiol groups (6.06% S atom), followed by SGO/Fe-Mn-ac (2.69% S atom) and SGO/Fe-Mn-ne (1.70% S atom). The elements of C, O, Si, S, Mn, and Fe were detected on the surface of these materials. The Fe and Mn relative atomic percentage of SGO/Fe-Mn decreased (the same for C and O) due to the addition of Si and S (present in 3-MPTS). The S atom percentage and S/C ratio followed the order of SGO/Fe-Mn-am (6.06%, 0.11) > SGO/Fe-Mn-ac (2.69%, 0.04) > SGO/Fe-Mn-ne (1.70%, 0.03), indicating the promoting effects of CH_3-COOH and NH_4OH during the thiol-functionalization. The Fe/Mn ratio of SGO/Fe-Mn-ac (7.00) is obviously different from GO/Fe-Mn (1.47) [26]. In contrast, SGO/Fe-Mn-am and SGO/Fe-Mn-ne maintained a similar Fe/Mn proportions (1.52 and 1.62) to GO/Fe-Mn.

The XPS spectra of C1s is shown in Fig. 6. The peaks of C1s for GO/Fe-Mn at 283.0, 284.1, 286.2, 287.8, and 288.6 eV were ascribed to C—Fe, C—C/C=C, C—O, C=O, and O—C=O [40,41], which were also observed in three SGO/Fe-Mn. After thiol-functionalization, C—Fe decreased from 1.0% for GO/Fe-Mn to 0.95% and 0.98% for SGO/Fe-Mn-ac and SGO/Fe-Mn-ne, respectively, while increased to 1.6% for SGO/Fe-Mn-am. For SGO/Fe-Mn-ac, SGO/Fe-Mn-ne, and SGO/Fe-Mn-am, C—C/C=C increased from 52.9% for GO/Fe-Mn to 55.6%, 54.5%, and 70.7%, C—O decreased from 37.7% for GO/Fe-Mn to 32.8%, 32.6%, and 19.4%, respectively. C=O decreased from 4.3% for GO/Fe-Mn to 3.7% for SGO/Fe-Mn-ac while increased to 8.6% and 4.9% for SGO/Fe-Mn-ne and SGO/Fe-Mn-am, respectively. O—C=O increased from 3.7% (at 288.6 eV) for GO/Fe-Mn to 5.6% (shifted to 288.7 eV) for SGO/Fe-Mn-ac while decreased to 2.8% (shifted to 289.0 eV) for SGO/Fe-Mn-ne and 2.5% (shifted to 288.8 eV) for SGO/Fe-Mn-am. The change of the O—C=O may be related to the acidity/basicity of the solution during the preparation. The binding energy of C—O shifted from 286.2 eV for GO/Fe-Mn to 286.1 eV for three SGO/Fe-Mn, C=O shifted from 287.8 eV for GO/Fe-Mn to 287.6 eV (SGO/Fe-Mn-ac) and 287.4 eV (SGO/Fe-Mn-ne and SGO/Fe-Mn-am). The results above indicated that 3-MPTS were coated on the surface of GO/Fe-Mn through oxygen-containing functional groups (i.e., C—O, C=O, and O—C=O) and π-π interactions.

The Fe2p (Fig. 7) peaks of GO/Fe-Mn at 706.0, 709.1, 710.5, 712.5, 716.7, 719.3, and 723.8 eV were characteristic of Fe_3C, FeO, Fe_2O_3, FeOOH, Fe^{2+} $2p_{3/2}$ satellite peak, Fe^{3+} $2p_{3/2}$ fingerprint peak, and $Fe2p_{1/2}$, respectively [41–46]. Similar Fe2p peaks were also observed in the three SGO/Fe-Mn. After thiol-functionalization, Fe_3C decreased from 2.0% for GO/Fe-Mn (at 706.0 eV) to 0.6% (shifted to 707.3 eV) for SGO/Fe-Mn-ac, increased to 4.3% (shifted to 707.3 eV) for SGO/Fe-Mn-am, the variation trend of Fe_3C was consistent with the C—Fe for C1s. FeO decreased from 14.4% (at 709.1 eV) for GO/Fe-Mn to 11.0%, 14.1%, and 3.1% (shifted to 710.2, 709.7, and 708.6 eV), Fe_2O_3 decreased from 26.5% (at 710.5 eV) for GO/Fe-Mn to 10.2%, 6.2%, and 8.1% (shifted to 711.3, 710.9, and 710.0 eV) for SGO/Fe-Mn-ac, SGO/Fe-Mn-ne, and SGO/Fe-Mn-am, respectively. While FeOOH increased from 29.0% for GO/Fe-Mn (at 712.5 eV) to 50.8%, 47.1%, and 52.4% (shifted to 712.6, 711.8, and 711.7 eV) for SGO/Fe-Mn-ac, SGO/Fe-Mn-ne, and SGO/Fe-Mn-am, respectively. The results indicated that Fe_3C, FeO, Fe_2O_3, and FeOOH took part in the process of thiol-functionalization, and the addition of 3-MPTS promoted the formation of FeOOH (especially in the presence of CH_3COOH and NH_4OH) while decreased the ratio of Fe_2O_3. In addition, CH_3COOH and NH_4OH promoted the corrosion of FeO with partial oxidation of Fe^{2+} to Fe^{3+}.

The Mn2p (Fig. 8) peaks at 638.3, 639.9, 641.5, 644.5, 647.6 and 652.3 eV for GO/Fe-Mn are ascribed to Mn(0), Mn^{2+} for MnO, Mn^{3+} for MnOOH, Mn^{4+} for MnO_2, Mn^{2+} $2p_{3/2}$ satellite peak, and $Mn2p_{1/2}$ [45,47]. For SGO/Fe-Mn-ac, SGO/Fe-Mn-ne, and SGO/Fe-Mn-am,

Table 1
The atomic percentage of GO/Fe-Mn [26] and three SGO/Fe-Mn from XPS data.

Adsorbent	C%	O%	Si%	S%	Mn%	Fe%	Fe/Mn	S/C
GO/Fe-Mn	66.96	29.65	1.37	0	0.64	0.94	1.47	0
SGO/Fe-Mn-ac	65.44	27.18	3.89	2.69	0.10	0.70	7.00	0.04
SGO/Fe-Mn-ne	65.78	28.88	2.34	1.70	0.50	0.81	1.62	0.03
SGO/Fe-Mn-am	57.86	27.88	7.63	6.06	0.23	0.35	1.52	0.11

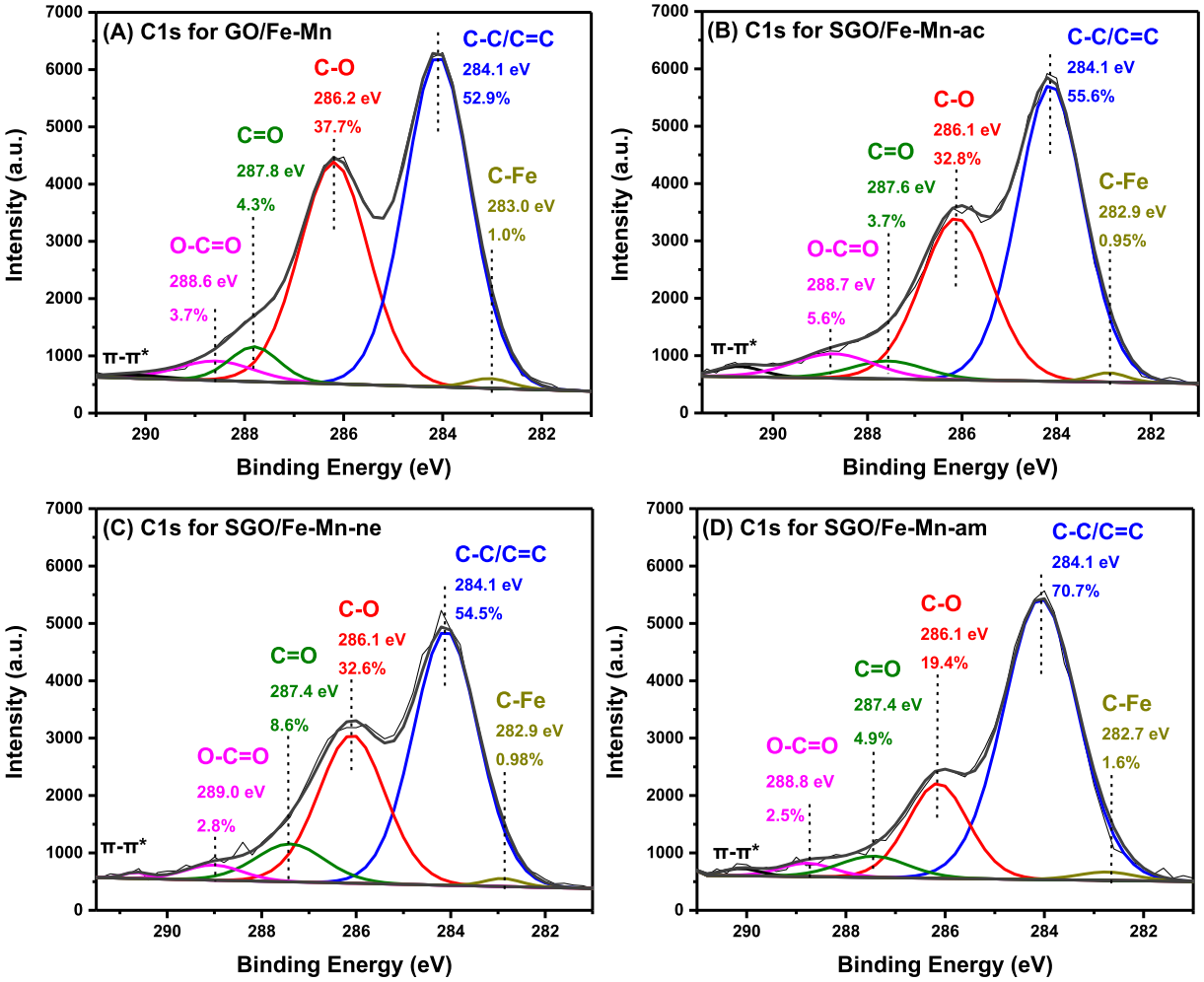

Fig. 6. XPS spectra of C1s for GO/Fe-Mn and three SGO/Fe-Mn: (A) GO/Fe-Mn, (B) SGO/Fe-Mn-ac, (C) SGO/Fe-Mn-ne, and (D) SGO/Fe-Mn-am.

Mn(0) and MnO_2 increased while MnO and MnOOH decreased, indicating the occurrence of oxidation-reduction reactions and the addition of 3-MPTS promoted the formation of Mn(0) (especially in the presence of NH_4OH) and MnO_2 (especially in the presence of NH_4OH or at neutral) while decreased the ratio of MnO (especially in the presence of CH_3COOH and NH_4OH) and MnOOH. For instance, Mn(0) and MnO_2 increased from 1.5% and 17.2% for GO/Fe-Mn to 7.6% and 22.8% for SGO/Fe-Mn-am, MnO and MnOOH decreased from 8.6% and 48.0% for GO/Fe-Mn to 2.4% and 44.5% for SGO/Fe-Mn-am. Binding energy of Mn(0), MnO, MnOOH, and MnO_2 shifted from 638.3, 639.9, 641.5, and 644.5 eV for GO/Fe-Mn to 638.1, 640.3, 641.3, and 644.7 eV for SGO/Fe-Mn-am.

The S2p (Fig. 9A–C) binding energies of SGO/Fe-Mn-ac at 163.6, 162.6, 167.5, and 160.2 eV were representative of $S2p_{1/2}$ (—SH), $S2p_{3/2}$ (—SH), oxidized sulfur (e.g., thiosulfate, sulfite) and sulphides (e.g., FeS, Fe_2S_3), respectively [46,48]. For SGO/Fe-Mn-ac, SGO/Fe-Mn-ne, and SGO/Fe-Mn-am, oxidized sulfur were 16.7%, 20.2%, and 14.5%, sulphides were 3.2%, 2.2%, and 1.0%, —SH were 82.2%, 77.6%, and 84.4%, respectively, indicating that thiol groups were the dominant sulfur forms in SGO/Fe-Mn (especially in SGO/Fe-Mn-ac and SGO/Fe-Mn-am), and that CH_3COOH promoted the formation of sulphides while NH_4OH restrained. The Si2p (Fig. 9D–F) binding energy of SGO/Fe-Mn-ac at around 98.9, 101.2, and 101.9 eV represented Si(0)/Si—Fe, Si—O—Si, and C—O—Si/Si—O—M (M = Fe or Mn), respectively, and there was a new binding energy at 103.4 eV (7.7%) attributing to SiO_2 for SGO/Fe-Mn-ne [46,49,50]. Si(0)/Si—Fe was fewest for SGO/Fe-Mn-am (2.5%) comparing with SGO/Fe-Mn-ac (6.3%) and SGO/Fe-Mn-ne (6.5%). C—O—Si/Si—O—M for SGO/Fe-Mn-ne (75.3%) was more than SGO/Fe-Mn-ac (57.0%) and SGO/Fe-Mn-am (48.9%), while Si—O—Si for SGO/Fe-Mn-am (48.6%) was more than SGO/Fe-Mn-ac (36.7%) and SGO/Fe-Mn-ne (7.8%), indicating hydrolyzed 3-MPTS mainly combined with oxygen-containing functional groups (e.g., C—O, O—C=O) and metal oxides, partially through 3-MPTS self-polymerization, which accounted for a larger proportion for SGO/Fe-Mn-am than SGO/Fe-Mn-ac and SGO/Fe-Mn-ne.

The XPS results above indicated that, after thiol-functionalization, Fe_2O_3, FeOOH, FeO, Fe_3C, Mn(0), MnO_2, MnO and MnOOH were the dominant metal compounds. Fe-Mn oxides which were coated on the GO surface provided abundant hydroxyl groups (e.g., FeOOH, MnOOH) for surface thiol-modification with 3-MPTS. The three SGO/Fe-Mn (especially SGO/Fe-Mn-am) showed weaker C1s, Fe2p, Mn2p peak intensities than GO/Fe-Mn, which may be due to the surface coating of the abundant 3-MPTS. The relative peak intensity ratio of oxygen-containing functional groups to C—C/C=C for SGO/Fe-Mn were lower than GO/Fe-Mn, further confirmed the occupation of surface oxygen-containing functional groups with strong π-π band. SGO/Fe-Mn-am showed stronger S2p and Si2p peak intensities than SGO/Fe-Mn-ac and SGO/Fe-Mn-ne due to more 3-MPTS coating.

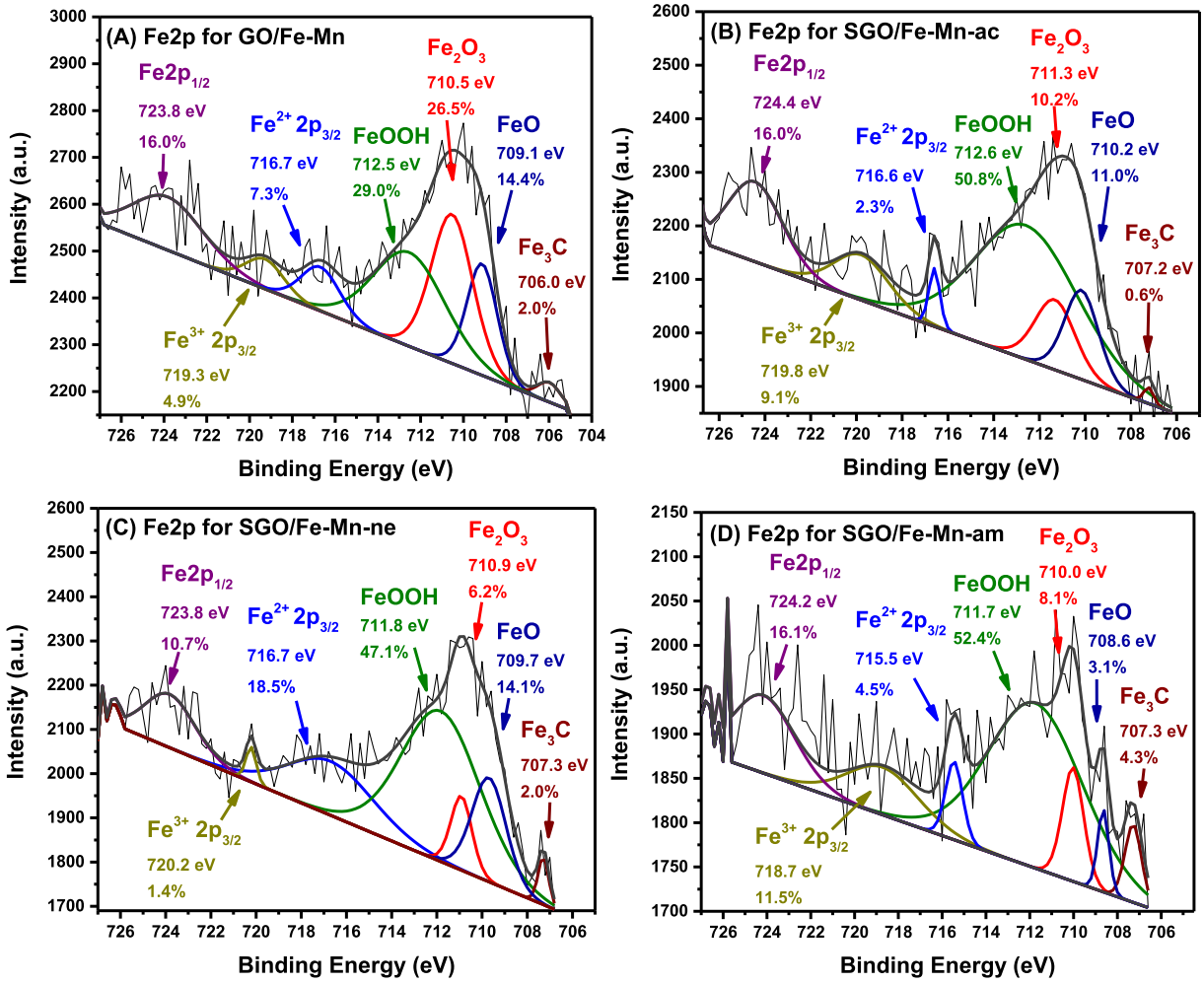

Fig. 7. XPS spectra of Fe2p for GO/Fe-Mn and three SGO/Fe-Mn: (A) GO/Fe-Mn, (B) SGO/Fe-Mn-ac, (C) SGO/Fe-Mn-ne, and (D) SGO/Fe-Mn-am.

3.2. Methylmercury sorption by GO/Fe-Mn and SGO/Fe-Mn

Methylmercury sorption (Fig. 10A) revealed a rapid initial rate in 1.5 h with 60.9–76.8% CH_3Hg^+ removal efficiency for three SGO/Fe-Mn, which can be explained by the fact that more accessible sorption sites were occupied first [51]. Then the sorption rate slowed down till equilibrium after 3 days with a CH_3Hg^+ removal efficiency of 86.4%, 81.3%, and 91.1% for SGO/Fe-Mn-ac, SGO/Fe-Mn-ne, SGO/Fe-Mn-am, respectively, which were about 4.7–5.3 times higher than GO/Fe-Mn (17.1%).

Pseudo-first-order and pseudo-second-order kinetic models were applied to simulate the kinetic data (Fig. 10B, C) and the resultant fitting parameters were summarized in Table S2. For SGO/Fe-Mn-ac, SGO/Fe-Mn-ne, SGO/Fe-Mn-am, and GO/Fe-Mn, the pseudo-second-order kinetic model provided better fitting (R^2 = 0.999 for all the four materials) than the pseudo-first-order model (R^2 = 0.864, 0.776, 0.717, and 0.890), suggesting that chemisorption was the rate limiting step rather than diffusion [52].

Fig. 10D depicts CH_3Hg^+ sorption isotherms of SGO/Fe-Mn and GO/Fe-Mn at a fixed pH of 7.0 ± 0.2 and room temperature (25 ± 2 °C). Langmuir and Freundlich isotherm models were applied to fit the experimental data, and the fitting results are compared in Table S3. Freundlich isotherm model describes nonideal sorption on heterogeneous surfaces as well as multilayer sorption, and Langmuir isotherm model depicts monolayer sorption [53]. For SGO/Fe-Mn-ac, SGO/Fe-Mn-ne, SGO/Fe-Mn-am, and GO/Fe-Mn, Langmuir model (R^2 = 0.991, 0.993, 0.986, and 0.998) and Freundlich model (R^2 = 0.996, 0.998, 0.996, and 0.999) fitted well. It should be noted that Freundlich isotherm model fitted better at low equilibrium methylmercury concentrations and Langmuir isotherm fitted better at high concentrations [53]. Therefore, the sorption behavior may be described as a non-ideal sorption on heterogeneous surfaces and multilayer sorption at low methylmercury concentration, while a monolayer adsorption at high concentration [53]. SGO/Fe-Mn offered much greater CH_3Hg^+ maximum sorption capacity (SGO/Fe-Mn-am: 43.88 ± 3.38 mg/g, SGO/Fe-Mn-ac: 36.33 ± 2.78 mg/g, SGO/Fe-Mn-ne: 28 ± 1.90 mg/g) than some reported carbon-based materials, such as chitosan ($q_e = 6.00 \times 10^{-3}$ mg/g) [2], barbital immobilized chitosan ($q_e = 1.00 \times 10^{-2}$ mg/g) [2], glutaraldehyde cross-linked chitosan ($q_e = 8.90 \times 10^{-3}$ mg/g) [12], barbital-glutaraldehyde cross-linked chitosan ($q_e = 7.20 \times 10^{-3}$ mg/g) [12], *Coriandrum sativum* biosorbent (q_e = 7.00 mg/g) [13], *Lemna minor* powder ($q_e = 2.80 \times 10^{-2}$ mg/g) [15], and rasped pith sago residue biosorbent (q_e = 42.80 mg/g) [14].

Among the three kinds of SGO/Fe-Mn, SGO/Fe-Mn-am demonstrated the highest maximum methylmercury sorption capacity, which might be closely related to the surface structure and functional groups. Thiol groups (—SH) exhibits a strong binding affinity for mercury, and hydroxyl groups (—OH) of metal oxides and functional groups (C=O, epoxy C—O—C, carboxyl O=C—O and C—O) of GO can immobilize mercury through ligand exchange and surface complexation [20,21,26,30]. SGO/Fe-Mn surface was negatively charged at pH 7, and electrostatic attraction may be another

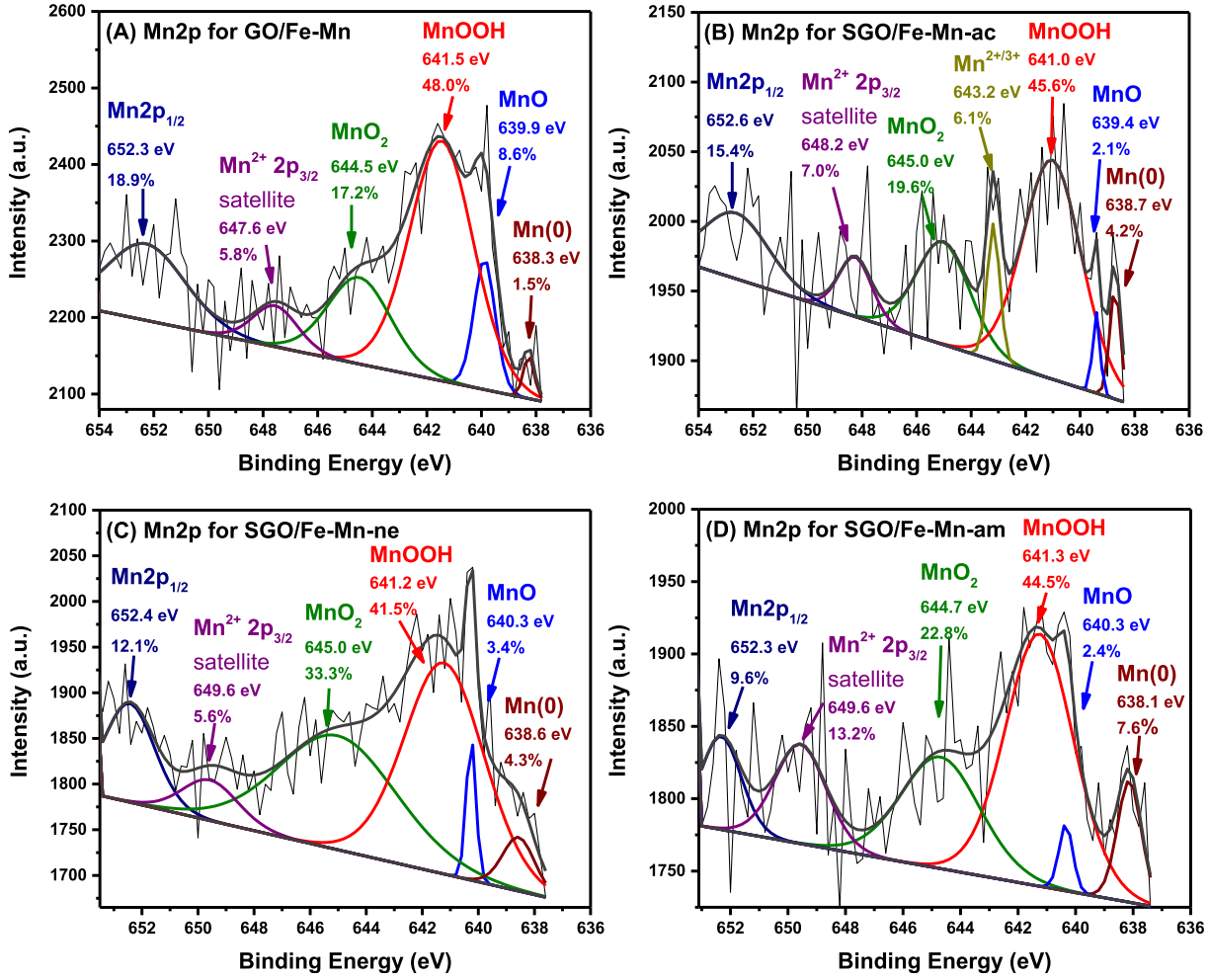

Fig. 8. XPS spectra of Mn2p for GO/Fe-Mn and three SGO/Fe-Mn: (A) GO/Fe-Mn, (B) SGO/Fe-Mn-ac, (C) SGO/Fe-Mn-ne, and (D) SGO/Fe-Mn-am.

mechanism, in addition, cation CH_3Hg^+ in solution can form cation-π interaction with sp^2-type groups (e.g., C═C, C—O—C, C═O, and O═C—O) through electrostatic attraction or polarization interaction [54]. More thiol groups, sp^3 defects (related to self-polymerization of 3-MPTS), hydroxyl groups (e.g., FeOOH), negative charges, and stronger π-π bond were observed in SGO/Fe-Mn-am as discussed in Section 3.1, resulting in the highest CH_3Hg^+ adsorption capacity (43.88 ± 3.38 mg/g) among the three kinds of SGO/Fe-Mn.

4. Conclusions

In this study, a novel thiol-functionalized GO/Fe-Mn composite (SGO/Fe-Mn) was synthesized via three different methods, i.e., acid method, neutral method, and ammonium hydroxide method, and compared for aqueous methylmercury (CH_3Hg^+) removal effectiveness. The primary findings are summarized as follows:

(1) SGO/Fe-Mn was formed mainly through the interaction between hydrolyzed 3-MPTS and surface oxygen-containing groups of GO/Fe-Mn (i.e., —OH, C═O, epoxy C—O—C, carboxyl O═C—O, and C—O) and π-π interactions, partially through self-polymerization of hydrolyzed 3-MPTS.
(2) After thiol-functionalization, Fe_2O_3, FeOOH, FeO, Fe_3C, Mn (0), MnO_2, MnO, and MnOOH were dominant metal compounds in SGO/Fe-Mn. Compared with GO/Fe-Mn, SGO/Fe-Mn (especially SGO/Fe-Mn-am) possessed larger hydrodynamic diameters, stronger π-π bond, more sp^3 defects and FeOOH. Among three SGO/Fe-Mn, SGO/Fe-Mn-am had the fewest S oxidation products, most thiol groups, and most negative charge, followed by SGO/Fe-Mn-ac and SGO/Fe-Mn-ne.
(3) Sorption kinetic tests indicated a fairly rapid methylmercury sorption rate of SGO/Fe-Mn with an equilibrium time of 48 h. A pseudo-second-order kinetic model was able to adequately interpret the rate data, indicating that chemisorption was the rate limiting step rather than diffusion. Langmuir and Freundlich isotherm model fitted well with methylmercury sorption isotherm data. The equilibrium behavior can be described as a non-ideal sorption on heterogeneous surfaces. SGO/Fe-Mn-am offers the greatest CH_3Hg^+ maximum sorption capacity (43.88 ± 3.38 mg/g), followed by SGO/Fe-Mn-ac (36.33 ± 2.78 mg/g) and SGO/Fe-Mn-ne (28.00 ± 1.90 mg/g). All these values obviously higher than most of the reported carbon-based adsorbents.
(4) Zeta potential, FTIR, XPS, and sorption tests analysis indicated that the possible CH_3Hg^+ removal mechanisms by SGO/Fe-Mn were electrostatic attraction, ligand exchange, and surface complexation through surface active sites (i.e., thiol groups, oxygen-containing functional groups, and π-π bond).

SGO/Fe-Mn-am prepared via ammonium hydroxide method demonstrated the highest maximum sorption capacity of CH_3Hg^+.

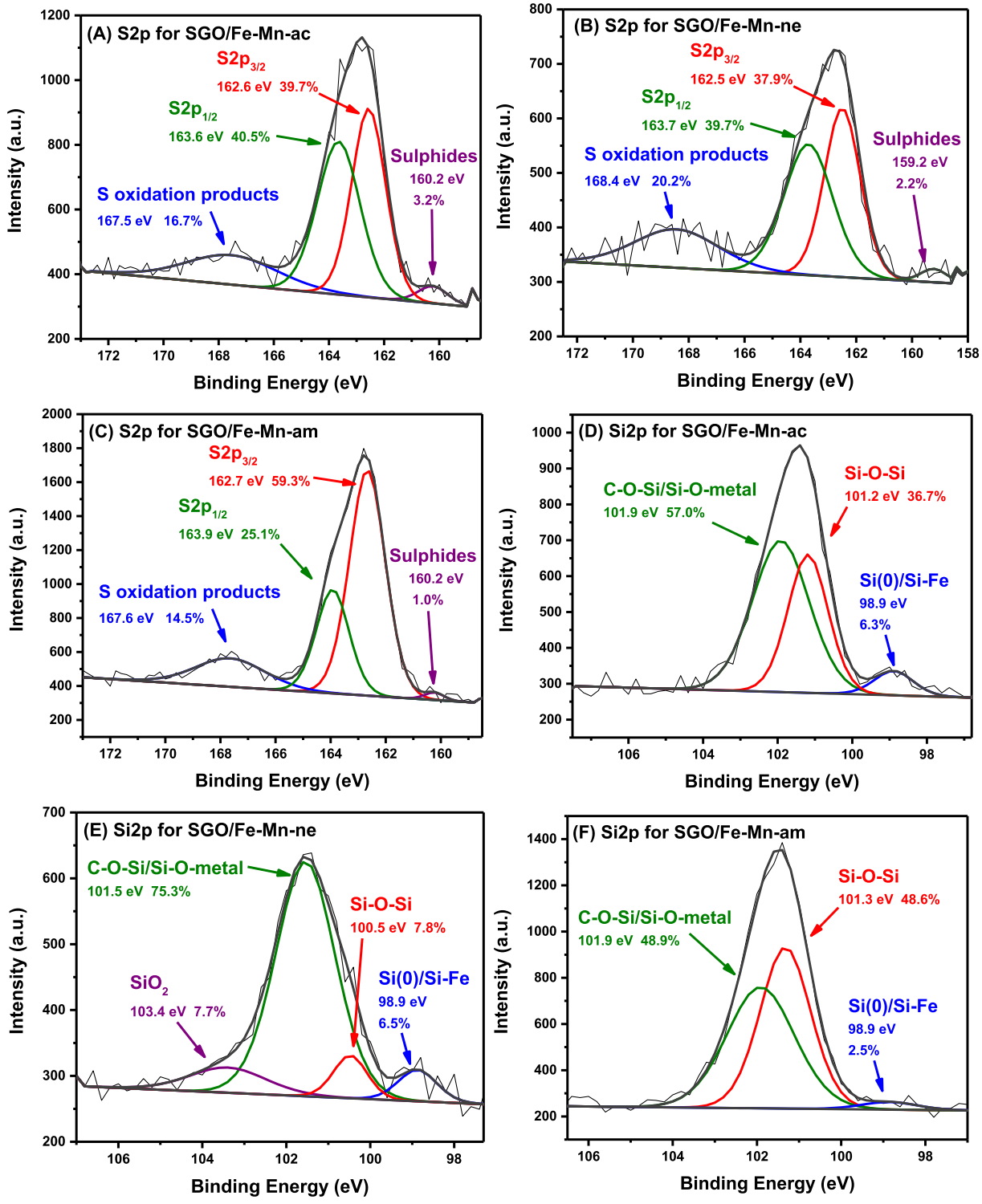

Fig. 9. XPS spectra of S2p and Si2p for three SGO/Fe-Mn: (A, D) SGO/Fe-Mn-ac, (B, E) SGO/Fe-Mn-ne, and (C, F) SGO/Fe-Mn-am.

This study demonstrates potential and viability of thiol-functionalized GO/Fe-Mn for enhanced immobilization of CH_3Hg^+ in surface water, groundwater, and soil/sediments. Future research work need to be carried out about influence of various factors (e.g., pH, dissolved organic matter, temperature, ionic strength, and time) on the immobilization effectiveness of aqueous CH_3Hg^+ by SGO/Fe-Mn-am, underlying immobilization mechanisms, and regeneration of the adsorbent.

Acknowledgements

This work was supported by National Natural Science Foundation of China (41503085, 31270544), Scientific Research Foundation for Returned Overseas Chinese Scholars, Ministry of Education of China ([2015]1098), Tianjin Research Program of Application Foundation and Advanced Technology (15JCYBJC53800), and 863 achievement transformation program in Tianjin (No. 14RCHZSF00144).

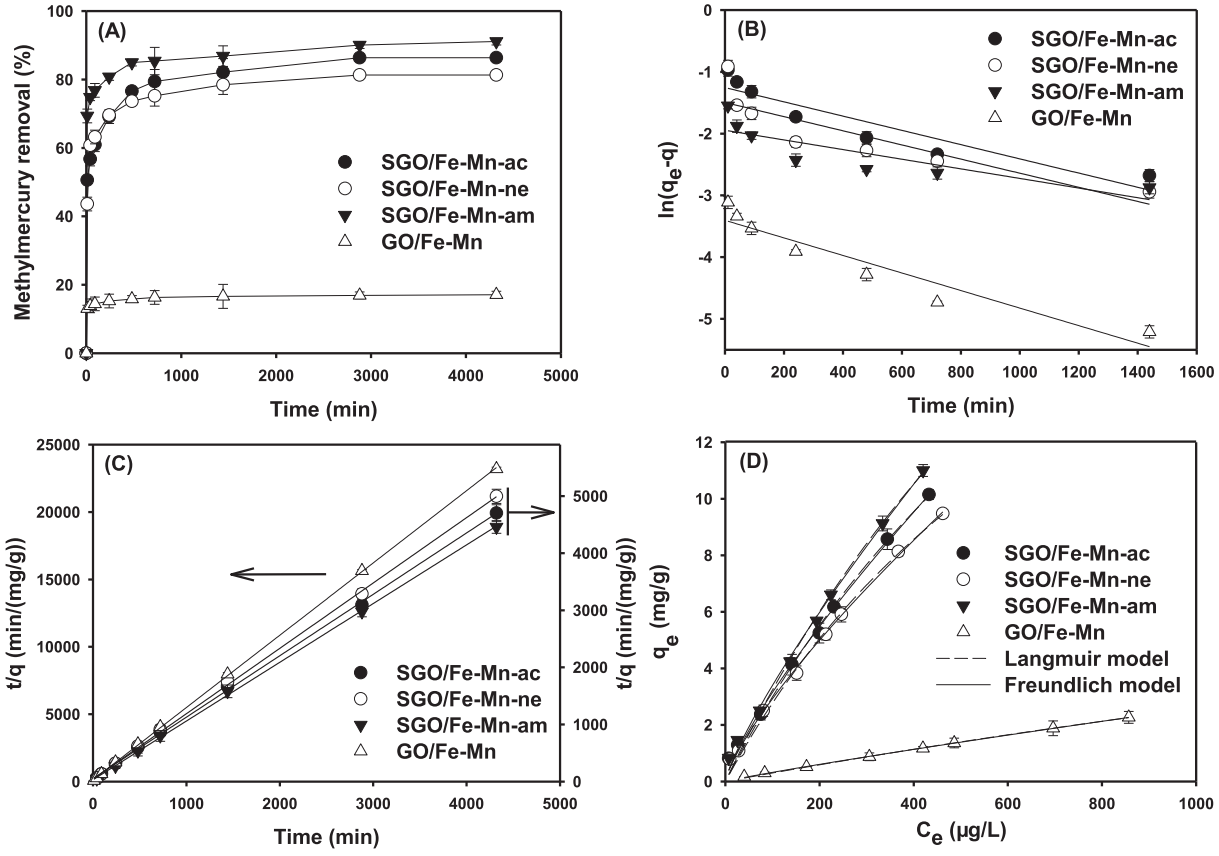

Fig. 10. (A) CH_3Hg^+ sorption kinetics, (B) pseudo-first-order kinetic model and (C) pseudo-second-order kinetic model fittings. Initial CH_3Hg^+ = 50 μg Hg/L, adsorbent dosage = 50 mg/L, pH = 7 ± 0.2, and ionic strength = 0.01 M $NaNO_3$. (D) CH_3Hg^+ sorption isotherm. Initial CH_3Hg^+ = 50–950 μg Hg/L, adsorbent dosage = 50 mg/L, pH = 7 ± 0.2, ionic strength = 0.01 M $NaNO_3$. Symbols: experimental data; lines: model fittings. Data plotted as mean of duplicates and the error bars (calculated as standard error) indicate data reproducibility.

Appendix A. Supplementary data

Supplementary data associated with this article can be found, in the online version, at http://dx.doi.org/10.1016/j.cej.2017.03.015.

References

[1] C.C. Gilmour, E.A. Henry, R. Mitchell, Sulfate stimulation of mercury methylation in freshwater sediments, Environ. Sci. Technol. 26 (1992) 2281–2287.
[2] S. Kushwaha, B. Sreedhar, P. Padmaja, Sorption of phenyl mercury, methyl mercury, and inorganic mercury onto chitosan and barbital immobilized chitosan: spectroscopic, potentiometric, kinetic, equilibrium, and selective desorption studies, J. Chem. Eng. Data 55 (2010) 4691–4698.
[3] S. Hamelin, M. Amyot, T. Barkay, Y. Wang, D. Planas, Methanogens: principal methylators of mercury in lake periphyton, Environ. Sci. Technol. 45 (2011) 7693–7700.
[4] R.Q. Yu, J.R. Flanders, E.E. Mack, R. Turner, M.B. Mirza, T. Barkay, Contribution of coexisting sulfate and iron reducing bacteria to methylmercury production in freshwater river sediments, Environ. Sci. Technol. 46 (2012) 2684–2691.
[5] R.P. Mason, J.R. Reinfelder, F.M.M. Morel, Uptake, toxicity, and trophic transfer of mercury in a coastal diatom, Environ. Sci. Technol. 30 (1996) 1835–1845.
[6] P. Seller, C.A. Kelly, J.W.M. Rudd, A.R. MacHutchon, Photodegradation of methylmercury in lakes, Nature 380 (1996) 694–697.
[7] M.C. Sheehan, T.A. Burke, A. Navas-Acien, P.N. Breysse, J. McGready, M.A. Fox, Global methylmercury exposure from seafood consumption and risk of developmental neurotoxicity: a systematic review, Bull. W. H. O. 92 (2014) 254F–269F.
[8] WHO, Children's Health and the Environment, in: W.H. Organization (Ed.), 2008.
[9] USEPA, Mercury Study Report to Congress, in: U.S.E.P. Agency (Ed.), 1997.
[10] L. Cabral, P. Giovanella, A. Kerlleman, C. Gianello, F. Menezes Bento, F.A.O. Camargo, Impact of selected anions and metals on the growth and in vitro removal of methylmercury by Pseudomonas putida V1, Int. Biodeterior. Biodegrad. 91 (2014) 29–36.
[11] Y.K. Henneberry, T.E. Kraus, J.A. Fleck, D.P. Krabbenhoft, P.M. Bachand, W.R. Horwath, Removal of inorganic mercury and methylmercury from surface waters following coagulation of dissolved organic matter with metal-based salts, Sci. Total Environ. 409 (2011) 631–637.
[12] S. Kushwaha, P.P. Sudhakar, Adsorption of mercury(II), methyl mercury(II) and phenyl mercury(II) on chitosan cross-linked with a barbital derivative, Carbohydr. Polym. 86 (2011) 1055–1062.
[13] D. Karunasagar, M.V. Krishna, S.V. Rao, J. Arunachalam, Removal and preconcentration of inorganic and methyl mercury from aqueous media using a sorbent prepared from the plant Coriandrum sativum, J. Hazard. Mater. 118 (2005) 133–139.
[14] N. Saman, K. Johari, S.S. Tien, H. Mat, Removal of Hg(II) and $CH_3Hg(I)$ using rasped pith sago residue biosorbent, Clean Soil Air Water 42 (2014) 1541–1548.
[15] S.X. Li, F.Y. Zheng, H. Yang, J.C. Ni, Thorough removal of inorganic and organic mercury from aqueous solutions by adsorption on Lemna minor powder, J. Hazard. Mater. 186 (2011) 423–429.
[16] S. Feyte, A. Tessier, C. Gobeil, D. Cossa, In situ adsorption of mercury, methylmercury and other elements by iron oxyhydroxides and organic matter in lake sediments, Appl. Geochem. 25 (2010) 984–995.
[17] R. Ma, F. Cao, B. Liu, H. Hu, W. Gan, Synthesis of divinylbenzene polymer/Fe_3O_4 hybrid monolithic column for enrichment and online thermal desorption of methylmercury in real samples, Talanta 138 (2015) 138–143.
[18] O. Hakami, Y. Zhang, C.J. Banks, Thiol-functionalised mesoporous silica-coated magnetite nanoparticles for high efficiency removal and recovery of Hg from water, Water Res. 46 (2012) 3913–3922.
[19] W. Stumm, J.J. Morgan, Aquatic Chemistry, Wiley-Interscience, New York, 1995.
[20] F. Kazemi, H. Younesi, A.A. Ghoreyshi, N. Bahramifar, A. Heidari, Thiol-incorporated activated carbon derived from fir wood sawdust as an efficient adsorbent for the removal of mercury ion: Batch and fixed-bed column studies, Process Saf. Environ. Prot. 100 (2016) 22–35.
[21] A.S. Krishna Kumar, S.-J. Jiang, W.-L. Tseng, Facile synthesis and characterization of thiol-functionalized graphene oxide as effective adsorbent for Hg(II), J. Environ. Chem. Eng. 4 (2016) 2052–2065.
[22] F. He, W. Wang, J.W. Moon, J. Howe, E.M. Pierce, L. Liang, Rapid removal of Hg (II) from aqueous solutions using thiol-functionalized Zn-doped biomagnetite particles, ACS Appl. Mater. Interfaces 4 (2012) 4373–4379.

[23] A. Guimarães, V. Ciminelli, W. Vasconcelos, Smectite organofunctionalized with thiol groups for adsorption of heavy metal ions, Appl. Clay Sci. 42 (2009) 410–414.
[24] S. Zhang, Y. Zhang, J. Liu, Q. Xu, H. Xiao, X. Wang, H. Xu, J. Zhou, Thiol modified Fe_3O_4@SiO_2 as a robust, high effective, and recycling magnetic sorbent for mercury removal, Chem. Eng. J. 226 (2013) 30–38.
[25] B. Yu, X. Wang, W. Xing, H. Yang, X. Wang, L. Song, Y. Hu, S. Lo, Enhanced thermal and mechanical properties of functionalized graphene/thiol-ene systems by photopolymerization technology, Chem. Eng. J. 228 (2013) 318–326.
[26] J. Tang, Y. Huang, Y. Gong, H. Lyu, Q. Wang, J. Ma, Preparation of a novel graphene oxide/Fe-Mn composite and its application for aqueous Hg(II) removal, J. Hazard. Mater. 316 (2016) 151–158.
[27] A. Gupta, S.R. Vidyarthi, N. Sankararamakrishnan, Thiol functionalized sugarcane bagasse-a low cost adsorbent for mercury remediation from compact fluorescent bulbs and contaminated water streams, J. Environ. Chem. Eng. 2 (2014) 1378–1385.
[28] N. Fairley, http://www.casaxps.com/, © Casa Software Ltd, 2016.
[29] N. Fairley, http://www.casaxps.com/help_manual/line_shapes.htm, © Casa Software Ltd, 2016.
[30] C.J. Daughney, S.D. Siciliano, A.N. Rencz, D. Lean, D. Fortin, Hg(II) adsorption by bacteria: a surface complexation model and its application to shallow acidic lakes and wetlands in Kejimkujik National Park, Nova Scotia, Canada, Environ. Sci. Technol. 36 (2002) 1546–1553.
[31] J. Tang, H. Lv, Y. Gong, Y. Huang, Preparation and characterization of a novel graphene/biochar composite for aqueous phenanthrene and mercury removal, Bioresour. Technol. 196 (2015) 355–363.
[32] J. Wang, Z. Chen, B. Chen, Adsorption of polycyclic aromatic hydrocarbons by graphene and graphene oxide nanosheets, Environ. Sci. Technol. 48 (2014) 4817–4825.
[33] H. Lyu, Y. Gong, J. Tang, Y. Huang, Q. Wang, Immobilization of heavy metals in electroplating sludge by biochar and iron sulfide, Environ. Sci. Pollut. Res. Int. 23 (2016) 14472–14488.
[34] F. Ke, L.G. Qiu, Y.P. Yuan, F.M. Peng, X. Jiang, A.J. Xie, Y.H. Shen, J.F. Zhu, Thiol-functionalization of metal-organic framework by a facile coordination-based postsynthetic strategy and enhanced removal of Hg^{2+} from water, J. Hazard. Mater. 196 (2011) 36–43.
[35] P.N. Diagboya, B.I. Olu-Owolabi, D. Zhou, B.-H. Han, Graphene oxide-tripolyphosphate hybrid used as a potent sorbent for cationic dyes, Carbon 79 (2014) 174–182.
[36] R. Graupner, Raman spectroscopy of covalently functionalized single-wall carbon nanotubes, J. Raman Spectrosc. 38 (2007) 673–683.
[37] H. Wang, J.T. Robinson, X. Li, H. Dai, Solvothermal reduction of chemically exfoliated graphene sheets, J. Am. Chem. Soc. 131 (2009) 9910–9911.
[38] F. Yin, S. Wu, Y. Wang, L. Wu, P. Yuan, X. Wang, Self-assembly of mildly reduced graphene oxide monolayer for enhanced Raman scattering, J. Solid State Chem. 237 (2016) 57–63.
[39] D. Yang, A. Velamakanni, G. Bozoklu, S. Park, M. Stoller, R.D. Piner, S. Stankovich, I. Jung, D.A. Field, C.A. Ventrice, R.S. Ruoff, Chemical analysis of graphene oxide films after heat and chemical treatments by X-ray photoelectron and micro-Raman spectroscopy, Carbon 47 (2009) 145–152.
[40] H. Fu, D. Zhu, Graphene oxide-facilitated reduction of nitrobenzene in sulfide-containing aqueous solutions, Environ. Sci. Technol. 47 (2013) 4204–4210.
[41] T. Herranz, S. Rojas, M. Ojeda, F.J. Perez-Alonso, P. Terreros, K. Pirota, J.L.G. Fierro, Synthesis, structural features, and reactivity of Fe-Mn mixed oxides prepared by microemulsion, Chem. Mater. 18 (2006) 2364–2375.
[42] A.P. Grosvenor, B.A. Kobe, M.C. Biesinger, N.S. McIntyre, Investigation of multiplet splitting of Fe 2p XPS spectra and bonding in iron compounds, Surf. Interface Anal. 36 (2004) 1564–1574.
[43] R. Devaux, D. Vouagner, A.M. de Becdelievre, C. Duret-Thual, Electrochemical and surface studies of the ageing of passive layers grown on stainless steel in neutral chloride solution, Corros. Sci. 36 (1994) 171–186.
[44] Y. Zhang, M. Yang, X.-M. Dou, H. He, D.-S. Wang, Arsenate adsorption on an Fe-Ce bimetal oxide adsorbent: role of surface properties, Environ. Sci. Technol. 39 (2005) 7246–7253.
[45] M.C. Biesinger, B.P. Payne, A.P. Grosvenor, L.W.M. Lau, A.R. Gerson, R.S.C. Smart, Resolving surface chemical states in XPS analysis of first row transition metals, oxides and hydroxides: Cr, Mn, Fe, Co and Ni, Appl. Surf. Sci. 257 (2011) 2717–2730.
[46] C.D. Wagner, W.M. Riggs, L.E. Davis, J.F. Moulder, G.E. Muilenberg, Handbook of X-ray photoelectron spectroscopy, Perkin-Elmer Corporation Physical Electronics Division, 1979.
[47] J. Li, J. Chen, Y. Yu, C. He, Fe-Mn-Ce/ceramic powder composite catalyst for highly volatile elemental mercury removal in simulated coal-fired flue gas, J. Ind. Eng. Chem. 25 (2015) 352–358.
[48] R. Holm, X-ray Photoelectron Spectroscopy, Department of Applied Physics, Bayer AG, Leverkusen, Germany, pp. 37–72 (Chapter 2).
[49] L.N. Bui, M. Thompson, N.B. McKeown, A.D. Romaschin, P.G. Kalman, Surface modification of the biomedical polymer poly(ethylene terephthalate), Analyst 118 (1993) 463–474.
[50] B. Carriere, J.P. Deville, D. Brion, J. Escard, X-ray photoelectron study of some silicon-oxygen compounds, J. Electron Spectrosc. Relat. Phenom. 10 (1977) 85–91.
[51] L. Axe, P.R. Anderson, Sr diffusion and reaction within Fe oxides: evaluation of the rate-limiting mechanism for sorption, J. Colloid Interface Sci. 175 (1995) 157–165.
[52] Y.S. Ho, G. McKay, Pseudo-second order model for sorption processes, Process Biochem. 34 (1999) 451–465.
[53] Y.S. Ho, J.F. Porter, G. McKay, Equilibrium isotherm studies for the sorption of divalent metal ions onto peat: copper, nickel and lead single component systems, Water Air Soil Pollut. 141 (2002) 1–33.
[54] D.A. Dougherty, The cation–π interaction, Acc. Chem. Res. 46 (2013) 885–893.